

PAPER

Energy-resolved transport of ultracold atoms across the Anderson transition: theory and experiment

Jean-Philippe Banon^{1,2,3}, Sacha Barré¹, Ke Xie¹, Hoa Mai Quach¹, Xudong Yu¹, Yukun Guo¹, Myneni Niranjan¹, Alain Aspect¹, Vincent Josse¹, Nicolas Cherroret^{2,*}

¹ Université Paris-Saclay, Institut d'Optique Graduate School, CNRS, Laboratoire Charles Fabry, 91127, Palaiseau, France

² Laboratoire Kastler Brossel, Sorbonne Université, CNRS, ENS-PSL Research University, Collège de France, 4 Place Jussieu, 75005 Paris, France

³ Université Jean Monnet Saint-Etienne, CNRS, Institut d'Optique Graduate School, Laboratoire Hubert Curien, UMR 5516, Saint-Etienne F-42023, France

*Author to whom any correspondence should be addressed.

E-mail: nicolas.cherroret@lkb.upmc.fr

Abstract

In a recent experiment [X. Yu et al., arXiv:2602.07654], energy-resolved measurements of an atomic matter wave spreading in a speckle potential enabled the direct observation of the three-dimensional Anderson transition. In this work, we present a quantitative theoretical description of the matter-wave dynamics based on a tailored implementation of the self-consistent theory of localization, which incorporates both the spectral and spatial properties of the state prepared in the disorder. We benchmark this theoretical approach against *ab initio* numerical simulations, and use it to analyze the atom density profiles observed experimentally in the localized, diffusive, and critical regimes. Particular emphasis is placed on the key role of the atomic energy distribution, especially on the distinct contributions of Bose-condensed and thermal atoms to interpret the experimental profiles. Our framework provides a versatile and efficient theoretical toolbox for quantitatively describing wave-packet dynamics in three-dimensional disordered quantum systems, which remain challenging for state-of-the-art large-scale numerical simulations.

1 Introduction

Understanding quantum transport in disordered media is a long-standing challenge, central to condensed-matter [1], wave physics [2], and cold-atom experiments [3]. A key phenomenon in this context is Anderson localization, whereby interference effects suppress diffusion and can ultimately lead to the absence of transport [4, 5, 6]. Ultracold atoms provide a particularly powerful platform to investigate this physics, as disorder, dimensionality, and interactions can be controlled with high precision, while observables such as density profiles are directly accessible [7, 8, 9, 10, 11]. These capabilities have stimulated intense theoretical activity [12, 13, 14, 15, 16, 17, 18, 19, 20, 21, 22, 23, 24, 25, 26], and enabled experimental demonstrations of Anderson localization in one-dimensional [27, 28], two-dimensional [29] and three-dimensional (3D) [30, 31, 32, 33] disordered potentials, as well as precise studies of analogous dynamical localization phenomena in kicked-rotor systems [34, 35, 36, 37, 38, 39].

In a recent experiment [40], atoms were transferred using a radio-frequency (rf) scheme into a 3D disordered potential with a well-controlled and narrow energy distribution [41, 42]. This protocol enables the exploration of wave-packet dynamics at selected energies across the localized, diffusive, and critical regimes of the Anderson transition. In particular, it overcomes difficulties encountered in previous setups [30, 31, 32, 33], which were limited by a broad atomic energy distribution that prevented the direct observation of the transition and the study of the critical regime (see, e.g., Ref. [23]).

While the measurements reported in Ref. [40] provided a direct observation of the Anderson transition, a fully quantitative connection to microscopic theory remains to be established, in particular for an accurate description of the experimentally observed spatial density profiles. This calls for the development of a dedicated theoretical framework capable of reliably describing wave propagation over large distances and long time scales across the mobility edge in three dimensions. Such a framework must incorporate the key experimental

ingredients, notably the spatial and spectral properties of the initial states prepared by the rf transfer in the disorder.

In the present work, we undertake this task by developing a tailored implementation of the 3D self-consistent theory (SCT) of localization [43, 44, 45], designed to capture the above features of wave-packet dynamics. We first benchmark this approach against *ab initio* numerical simulations of 3D wave-packet spreading, which explicitly implement the rf-loading scheme and reproduce the statistical properties of the experimental speckle disorder. We then confront the theoretical predictions with experimental measurements of the density profiles across the mobility edge. This analysis reveals the central role of the atomic energy distribution in shaping the spatial structure of wave packets in the disordered potential.

The article is organized as follows. In Sec. 2, we recall the main elements of the experiment reported in Ref. [40], which enabled the realization of energy-resolved propagation of atomic wave packets in a disordered potential. We then develop a theoretical framework adapted to the experimental scenario, based on the SCT of localization. In Sec. 3, we benchmark this approach against *ab initio* numerical simulations performed under conditions close to those of the experiment. Section 4 is devoted to the comparison with the experimental measurements, including a characterization of the spatial and spectral distributions of the atomic cloud transferred into the disorder. In particular, we discuss the respective contributions of condensed and thermal atoms to the energy distribution. Finally, we summarize our findings and outline perspectives in Sec. 5.

2 Energy-resolved wave packet propagation across the Anderson transition: theory

2.1 Experimental context

In the experiment of Ref. [40], the dynamical spreading of ultracold atomic clouds prepared with well-defined energies in a three-dimensional random speckle potential was investigated in the vicinity of the Anderson mobility edge. Such energy-resolved transport was achieved using the scheme illustrated in Fig. 1: atoms from a Bose–Einstein condensate (BEC) are first

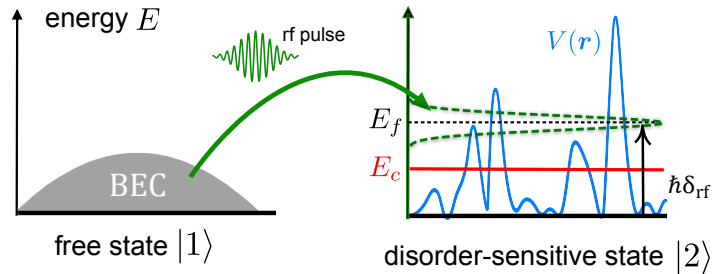


Figure 1. Experimental protocol of Ref. [40]: atoms from a Bose–Einstein condensate, initially prepared in a disorder-free state, are transferred to a disorder-sensitive state by means of an rf pulse. The transferred atoms acquire a narrow energy distribution (green dashed curve) centered at E_f , which can be tuned across the mobility edge E_c of the disordered potential.

prepared in a disorder-free hyperfine state $|1\rangle$, then transferred to a disorder-sensitive state $|2\rangle$ at a well-defined target energy $E_f = \hbar\delta_{\text{rf}}$. The transfer is driven by a radio-frequency pulse whose frequency sets the detuning δ_{rf} from the bare resonance of state $|2\rangle$. As shown in [40, 41], in the weak-coupling regime—where only a small fraction of the BEC is transferred—and provided that the condensate is large enough to be approximated by the uniform plane-wave state $|\mathbf{k} = 0\rangle$, the atoms loaded into the disorder acquire the following energy distribution:

$$\mathcal{D}(E; E_f) \simeq F(E - E_f)A(E, \mathbf{k} = 0). \quad (1)$$

Here $A(E, \mathbf{k} = 0)$ is the zero-momentum spectral function in the disordered potential, i.e., the probability density that an initial plane-wave state $|\mathbf{k} = 0\rangle$ has energy E in the random potential [41], and $F(E - E_f)$ is an energy-filter function determined by the temporal shape of the rf pulse. The filter is peaked around the target energy E_f , with a typical width $\Delta E = \hbar\delta_{\text{rf}} \ll E_f$. Note that the spectral function would correspond to the energy distribution obtained after an abrupt switch-on of the disorder applied to the BEC (see, e.g., Ref. [31]).

This protocol thus enables the preparation of atomic wave packets with much narrower energy distribution compared to previous experiments. Moreover, the targeted energy E_f can be finely tuned across the mobility edge E_c , enabling the precise investigation of the Anderson transition.

2.2 Energy-resolved state: model

Having introduced the experimental protocol, we now develop a simple model describing the preparation and the subsequent evolution of an energy-resolved state in the random potential. We denote by $|\phi\rangle$ the condensate wave function prior to the transfer, and by $|\psi_0\rangle$ the state of the atoms loaded into the disorder. For a coherent transfer, as realized in [40], we model the relation between these two states by

$$|\psi_0\rangle = f(\hat{H} - E_f)|\phi\rangle = \sum_n |\phi_n\rangle \langle \phi_n | \phi \rangle f(E_n - E_f), \quad (2)$$

where $\hat{H} = \mathbf{p}^2/(2m) + V(\mathbf{r})$ is the Hamiltonian in the disorder-sensitive state, with $V(\mathbf{r})$ the speckle potential, and $f(E - E_f)$ is an amplitude filter function such that $|f(E - E_f)|^2 \equiv F(E - E_f)$. In the second equality, we have introduced a complete set ($|\phi_n\rangle$) of eigenstates of \hat{H} with energies E_n , which will prove convenient in the following. One can easily verify that the definition (2) correctly yields the energy distribution (1) of the atoms in the disorder. Indeed, we have by definition

$$\begin{aligned} \mathcal{D}(E; E_f) &\equiv \overline{\langle \psi_0 | \delta(E - \hat{H}) | \psi_0 \rangle} \simeq |f(E - E_f)|^2 \sum_n \overline{|\langle \phi_n | \mathbf{k} = 0 \rangle|^2} \delta(E - E_n) \\ &\equiv F(E - E_f) A(E, \mathbf{k} = 0), \end{aligned} \quad (3)$$

where Eq. (2) has been used in the second equality, together with the approximation $|\phi\rangle \simeq |\mathbf{k} = 0\rangle$ for the condensate wave function in state |1). Here and in the following, the overbar denotes averaging over disorder realizations.

2.3 Disorder-averaged density

We now derive an expression for the disorder-averaged density $n(\mathbf{r}, t)$, suitable for the application of the self-consistent theory of localization, starting from the filtered initial state (2). The wave function $\psi(\mathbf{r}, t)$ of the cloud in the random potential at time t is related to the initial state $\psi(\mathbf{r}, t = 0) = \psi_0(\mathbf{r})$ by

$$\psi(\mathbf{r}, t) = \Theta(t) \langle \mathbf{r} | \exp(-i\hat{H}t) | \psi_0 \rangle = \Theta(t) \sum_n \langle \mathbf{r} | \phi_n \rangle \langle \phi_n | \phi \rangle f(E_n - E_f) \exp(-iE_n t), \quad (4)$$

where Θ is the Heaviside step function (unless otherwise stated, from now on we set $\hbar = 1$). By inserting the closure relation $\mathbf{1} = \int |\mathbf{r}'\rangle \langle \mathbf{r}'| d\mathbf{r}'$ and using the spectral representation

$$\Theta(t) f(E_n - E_f) \exp(-iE_n t) = -i \int \frac{dE}{2\pi} \frac{f(E - E_f) \exp(-iEt)}{E - E_n + i0}, \quad (5)$$

the wave function can be rewritten as

$$\psi(\mathbf{r}, t > 0) = -i \int \frac{dE}{2\pi} \int d\mathbf{r}' G^R(\mathbf{r}, \mathbf{r}', E) \phi(\mathbf{r}') f(E - E_f) \exp(-iEt), \quad (6)$$

where we have introduced the retarded Green's function

$$G^R(\mathbf{r}, \mathbf{r}', E) = \sum_n \frac{\langle \mathbf{r} | \phi_n \rangle \langle \phi_n | \mathbf{r}' \rangle}{E - E_n + i0}. \quad (7)$$

From Eq. (6), we obtain a general expression for the disorder-averaged density:

$$\begin{aligned} n(\mathbf{r}, t) &= \int d\mathbf{r}' d\mathbf{r}'' \int \frac{dE}{2\pi} \frac{d\omega}{2\pi} e^{-i\omega t} \overline{G^R(\mathbf{r}, \mathbf{r}', E_+) G^A(\mathbf{r}'', \mathbf{r}, E_-)} \phi(\mathbf{r}') \phi^*(\mathbf{r}'') \\ &\quad \times f(E_+ - E_f) f^*(E_- - E_f), \end{aligned} \quad (8)$$

where $G^A(\mathbf{r}'', \mathbf{r}, E) \equiv G^{R*}(\mathbf{r}, \mathbf{r}'', E)$ is the advanced Green's function, and we have changed the energy variables to $E \equiv (E_1 + E_2)/2$ and $\omega \equiv E_1 - E_2$, with $E_{\pm} = E \pm \omega/2$. Although Eq. (8) is fully general, it is not convenient for practical use, as it involves a correlator of Green's functions evaluated at three distinct spatial points. However, in the so-called hydrodynamic regime—where fast spatial and temporal variations of the profile (typically occurring on the scale of the mean free path and the mean free time, respectively) are neglected—this expression can be significantly simplified. The derivation is presented in Appendix A for clarity (see also Refs. [46, 10]), and leads to

$$n(\mathbf{r}, t) \simeq \int dE \int d\mathbf{r}' \mathcal{D}(E; E_f) P_E(\mathbf{r}, \mathbf{r}', t) |\phi(\mathbf{r}')|^2. \quad (9)$$

In this relation, $\mathcal{D}(E; E_f)$ is the energy distribution (1), and P_E is the disorder-averaged propagator, defined as

$$P_E(\mathbf{r}, \mathbf{r}', t) \equiv \frac{1}{2\pi\rho} \int \frac{d\omega}{2\pi} e^{-i\omega t} \overline{G^R(\mathbf{r}, \mathbf{r}', E_+) G^A(\mathbf{r}', \mathbf{r}, E_-)}, \quad (10)$$

with ρ the density of states per unit volume. Physically, P_E gives the probability density for a particle with energy E to propagate from \mathbf{r}' at time $t = 0$ to \mathbf{r} at time t in the random potential [47]. The averaged density (9) then follows by summing over all possible initial positions \mathbf{r}' and all energies, weighted by the energy distribution of the atoms. In the ideal limit of a very sharp filter function $F(E - E_f) \propto \delta(E - E_f)$, Eq. (9) further simplifies to

$$n(\mathbf{r}, t) \simeq \int d\mathbf{r}' P_{E_f}(\mathbf{r}, \mathbf{r}', t) |\phi(\mathbf{r}')|^2, \quad (11)$$

so that the density becomes a direct probe of transport in the disorder at energy E_f .

In Sec. 3, Eq. (11) will be compared with numerical simulations performed in the ideal sharp-filter limit. By contrast, when comparing with the experimental data in Sec. 4, it will be necessary to account for the finite width of the energy filter. We will therefore rely instead on Eq. (9).

2.4 Propagator: self-consistent theory

We now derive a general expression for the propagator P_E capturing the wave-packet dynamics across the mobility edge of the phase transition. To this end, we use the self-consistent theory of localization, a simple model in which the quantum interference responsible for Anderson localization are modeled by a re-summation of Cooper diagrams [43, 44, 45, 46]. Within this approach, the Fourier transform of the propagator (10) is given by

$$P_E(\mathbf{q}, \omega) = \frac{1}{-i\omega + D(\omega)q^2}, \quad (12)$$

involving a generalized diffusion coefficient $D(\omega)$ renormalized by quantum interference according to:

$$\frac{1}{D(\omega)} = \frac{1}{D_B} + \frac{1}{\pi\rho\hbar D_B} \int \frac{d\mathbf{Q}}{(2\pi)^3} \frac{1}{-i\omega + D(\omega)Q^2}, \quad (13)$$

where D_B is the so-called Boltzmann or classical diffusion coefficient and ρ the density of states. An exact calculation of the frequency-dependent diffusion coefficient $D(\omega)$ and the corresponding density $n(\mathbf{r}, t)$ was previously performed in [48] in one and two dimensions. Here, we extend this analysis to the 3D case. To this end, we first note that the integral on the right-hand side of Eq. (13) is divergent and must be regularized by introducing a UV cutoff Q_{UV} , typically of the order of the inverse mean free path. This can be conveniently achieved by isolating the divergence in the momentum integral as follows [49]:

$$\int \frac{d\mathbf{Q}}{2\pi^2 D(\omega)} \frac{Q^2 - i\omega/D(\omega) + i\omega/D(\omega)}{-i\omega/D(\omega) + Q^2} = \frac{1}{2\pi^2} \left[\int_0^{Q_{UV}} \frac{dQ}{D(\omega)} + \frac{i\omega}{D(\omega)} \int_0^{\infty} \frac{dQ}{-i\omega/D(\omega) + Q^2} \right]. \quad (14)$$

Carrying out the two integrals yields a third-order algebraic equation for $D(\omega)$, whose solution is

$$D(\omega) = \left[\beta \frac{-\alpha_0(1 - E/E_c) + [\sqrt{\alpha_0^3(1 - E/E_c)^3 - i\omega} + \sqrt{-i\omega}]^{2/3}}{[\sqrt{\alpha_0^3(1 - E/E_c)^3 - i\omega} + \sqrt{-i\omega}]^{1/3}} \right]^2, \quad (15)$$

where $\beta = (8\pi^2\rho\hbar)^{-1/3}$ and $\alpha_0(1 - E/E_c) = D_B[Q_{UV}/(2\pi^3\rho D_B\hbar) - 1]/(3\beta^2)$ (restoring \hbar). In this formulation, the three physical quantities ρ , D_B and Q_{UV} of the model are recast in terms of the three composite parameters α_0 , β and E_c . The latter, in particular, represents the mobility edge. While these parameters can be approximately estimated using perturbation theory [47, 50, 51], they are difficult to determine accurately in the strong-disorder regime where the Anderson transition occurs. Here we will therefore simply take them as constant free parameters of the theory, exploiting that they vary smoothly with energy E in the vicinity of the mobility edge we are focusing on. Together, Eqs. (1), (9), (12) and (15) provide a complete description of the wave-packet density at any position and time across the critical point. It is nevertheless instructive, at this stage, to recall the predictions of the theory in the limit of asymptotically long times, corresponding to $\omega \rightarrow 0$ [52]:

$$D(\omega) \underset{\omega \rightarrow 0}{\simeq} \begin{cases} 3\beta^2\alpha_0 \left(\frac{E}{E_c} - 1 \right) \equiv D_0 & E > E_c \\ \beta^2(-4i\omega)^{1/3} & E = E_c \\ -i\omega \frac{4\beta^2}{9\alpha_0^2(1 - E/E_c)^2} \equiv -i\omega\xi^2 & E < E_c \end{cases} \quad (16)$$

In terms of wave-packet spreading, these frequency scaling laws imply fundamentally different dynamics around the mobility edge, which can be traced in the time evolution of the mean squared width of the wave-packet, $\langle \mathbf{r}^2(t) \rangle \equiv \int d\mathbf{r} \mathbf{r}^2 n(\mathbf{r}, t)$. Assuming a sharp filter function, so that the wave packet has a well defined energy E_f , $\langle \mathbf{r}^2(t) \rangle$ readily follows from Eqs. (11) and (12) :

$$\langle \mathbf{r}^2(t \rightarrow \infty) \rangle \simeq - \int \frac{d\omega}{2\pi} \nabla_{\mathbf{q}} \cdot \nabla_{\mathbf{q}} \frac{e^{-i\omega t}}{-i\omega + D(\omega \rightarrow 0)\mathbf{q}^2} \Big|_{\mathbf{q}=0} = \int \frac{d\omega}{2\pi} \frac{6D(\omega \rightarrow 0)e^{-i\omega t}}{(-i\omega + 0^+)^2}. \quad (17)$$

Inserting the asymptotic laws (16), we infer:

$$\langle \mathbf{r}^2(t \rightarrow \infty) \rangle \propto \begin{cases} t & E > E_c \\ t^{2/3} & E = E_c \\ \text{const.} & E < E_c, \end{cases} \quad (18)$$

which are the usual diffusive, anomalous and localized behavior expected above, at and below the mobility edge [5, 53].

3 Benchmarking of the theory against numerical simulations

Before analyzing experimental results of Ref. [40] within the theoretical framework introduced in the previous section, we first assess its validity through comparison with *ab initio* numerical simulations. These simulations are performed in an idealized setting assuming sharp energy filtering and a spatially narrow initial state, yet under conditions close to those of the experiment. To this end, we numerically prepare, in a blue-detuned speckle potential $V(\mathbf{r})$, an initial filtered state $|\psi_0\rangle$ of the form given in Eq. (2), and then compute its time evolution $\psi(\mathbf{r}, t)$ in the random potential. The density $|\psi(\mathbf{r}, t)|^2$ is monitored as a function of time and subsequently averaged over disorder realizations, yielding the averaged density $n(\mathbf{r}, t) \equiv |\overline{\psi(\mathbf{r}, t)}|^2$.

3.1 Speckle potential

The speckle potential $V(\mathbf{r})$ is generated numerically on a regular rectangular grid of volume $(100\mu\text{m})^3$, using a Fourier filtering method similar to the one described in Ref. [41]. The disorder corresponds to a blue-detuned laser speckle, as in Ref. [40], implying that the potential is strictly positive. Its statistical distribution follows the exponential law $P(V) = \exp(-V/V_R)/V_R \cdot \Theta(V)$ [7]. Here, V_R denotes the root-mean-square (rms) value of the disorder and is referred to the disorder amplitude. For laser speckle potentials, V_R also coincides with the mean value of the disorder, *i.e.*, $\overline{V} = V_R$. In the following we present numerical results for $V_R/h = 416\text{Hz}$, as in Ref. [40].

The speckle potential is generated to accurately reproduce the experimental configuration, where the speckle grains are elongated along the x axis (see Fig. 2). More precisely, the parameters are chosen such that the autocorrelation function $C(\Delta\mathbf{r}) = \overline{\delta V(\mathbf{r})\delta V(\mathbf{r} + \Delta\mathbf{r})}/V_R^2$

(where $\delta V \equiv V - V_R$) matches the experimental one both along the longitudinal x axis and in the transverse x - y plane. As shown in Fig. 2c, the agreement between the numerical computation, the theoretical expression given by Eq. (42) in the Appendix C.1, and the experimental measurements [41, 40] of the autocorrelation, is excellent. Consistently with Ref. [23], the correlation lengths are defined as the half width at half maximum (HWHM) divided by a factor 1.39156. It yields $\sigma_x = 1.45 \mu\text{m}$ and $\sigma_\perp = 0.30 \mu\text{m}$ on the transverse plane. These correlation lengths set the correlation energy $E_\sigma = \hbar^2/m\sigma^2 = h \times 441 \text{ Hz}$, where $\sigma = 0.50 \mu\text{m}$ is the geometric mean over the different directions.

In the simulations, the discretization steps are typically $\Delta x = 0.7 \mu\text{m}$ and $\Delta y = \Delta z = 0.3 \mu\text{m}$, yielding $\sigma_x/\Delta x \approx 2$, $\sigma_\perp/\Delta z \approx 1$. These ratios are sufficient to properly resolve both the speckle grains [see Fig. 2(c)] and the de Broglie wavelength at the considered energies. Details of the numerical generation of the speckle potential and the theoretical form of the autocorrelation function are provided in Appendix C.1.

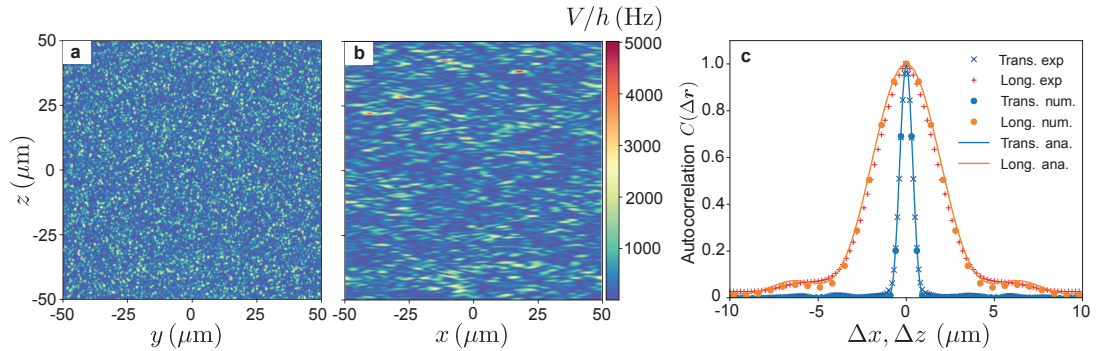


Figure 2. (a, b) Two-dimensional cuts of a realization of a three-dimensional speckle potential, and (c) its autocorrelation function along the longitudinal (x) and a transverse (z) directions. The speckle parameters are: $V_R/h = 416 \text{ Hz}$, $\sigma_x = 1.45 \mu\text{m}$, and $\sigma_\perp = 0.30 \mu\text{m}$. Crosses: experimental data; points: numerical data; solid lines: analytical autocorrelation function, Eq. (42). See Appendix C.1 for further details.

3.2 Numerical propagation of an energy-resolved wave-packet

To numerically prepare the initial state $|\psi_0\rangle$ defined by Eq. (2), we start from a Gaussian wave packet $\phi(\mathbf{r}) \propto \exp(-\mathbf{r}^2/4\Delta r^2)$, and consider a narrow Gaussian filter $f(E) \propto \exp[-(E - E_f)^2/4\Delta E^2]$, with $\Delta r = 3.5 \mu\text{m}$ and $\Delta E/h \simeq 4 \text{ Hz}$. The target energy E_f is varied around the expected mobility edge, typically from $E_f/h = 176$ to 376 Hz . To apply the filtering operation $f(\hat{H} - E_f)$ involved in Eq. (2), we do not compute the eigenstates of the random Hamiltonian, which would be numerically prohibitive for the 3D system considered here, but instead use an expansion of the operator $f(\hat{H} - E_f)$ on a basis of Chebyshev polynomials. This strategy was previously employed in Refs. [54, 55, 56] in the context of Anderson localization in momentum space, and is briefly described in Appendices C.2 and C.3.

Once the energy-resolved state $|\psi_0\rangle$ is computed following Eq. (2), we numerically propagate it in time by applying the time evolution operator $|\psi(t)\rangle = \exp(-i\hat{H}t)|\psi_0\rangle$. The time propagation is performed with high accuracy and efficiency using a Chebyshev expansion of the evolution operator, which is applied iteratively to obtain the state at successive time steps Δt . This method, briefly reviewed in Appendices C.2 and C.5, is more stable and efficient than Crank–Nicolson schemes, as it allows for relatively large time steps [57, 58]. Within this approach, we obtain the spatial density at time t , which we average over disorder realization to get the averaged density $n(\mathbf{r}, t)$.

To characterize the dynamics, we follow the methodology of Ref. [40] and we focus on the disorder-averaged linear density profile along z , defined as $n_{1d}(z, t) = \iint dx dy n(\mathbf{r}, t)$. Figure 3a–c shows such linear density profiles at different evolution times obtained from the numerical simulations (colored points) for three target energies E_f , corresponding respectively to the diffusive ($E_f > E_c$), critical ($E_f = E_c$) and localized regime ($E_f < E_c$). For the chosen numerical parameters, we estimate the mobility edge to be $E_c \simeq 264 \text{ Hz}$. This value slightly exceeds the numerical estimate $E_c \simeq 240 \text{ Hz}$ reported in Ref. [23], which is based on extensive transfer-matrix simulations. We attribute this discrepancy to the relatively coarse spatial discretization used in the present simulations, which is necessary to avoid the prohibitively

long computation times inherent to time-dependent expansion in a 3D disordered potential. Despite this, the simulation results clearly reveal the characteristic Gaussian spreading and the time-independent exponential profile expected on the diffusive (Fig. 3a) and localized (Fig. 3c) sides of the Anderson transition, respectively. Near the mobility edge (Fig. 3b), the profile exhibits an intermediate shape together with a slow expansion.

3.3 Comparison with the 3D self-consistent theory

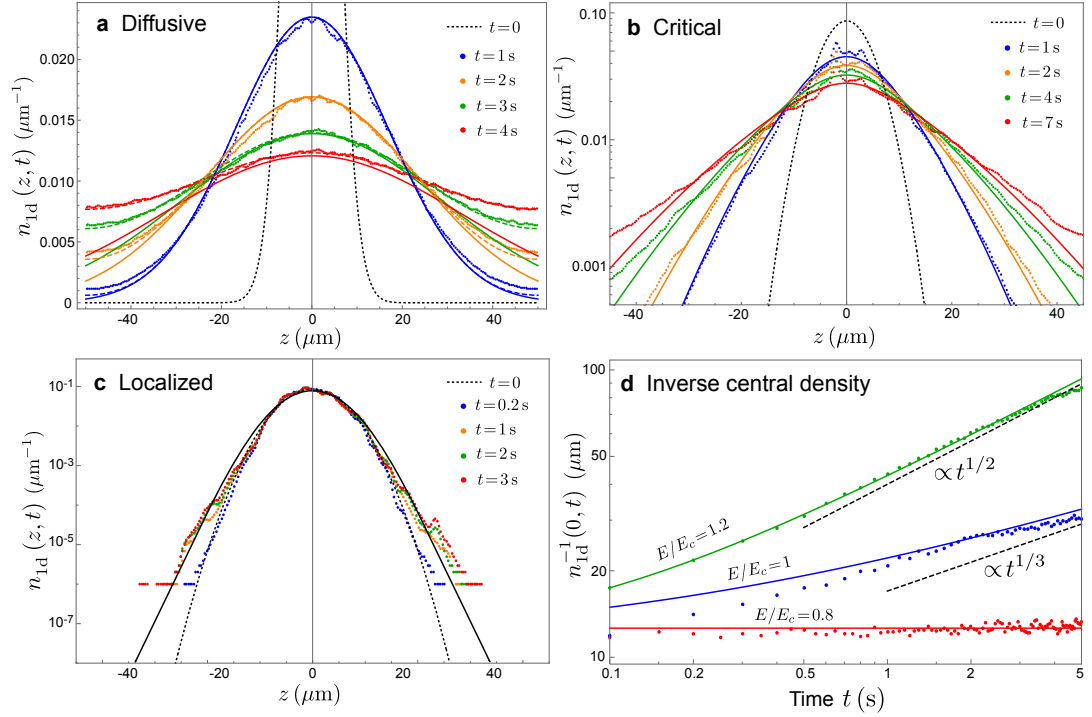


Figure 3. (a-c) Linear density profiles $n_{1d}(z, t)$ across the 3D Anderson transition in a speckle potential, obtained from numerical simulations of wave-packet propagation (discrete points) for a disorder characterized by the properties shown in Fig. 2. Three target energies are considered: (a) $E_f/h = 316$ Hz, (b) $E_f/h = 264$ Hz, and (c) $E_f/h = 216$ Hz, corresponding respectively to the diffusive, critical, and localized regimes. The solid lines show the long-time density profiles predicted by the SCT. In the diffusive regime (a), the colored dashed curves show the theoretical profiles including boundary corrections, Eq. (24). (d) Inverse of central density as a function of time for $E_f/h = 316$ Hz ($E/E_c \simeq 1.2$), $E_f/h = 264$ Hz ($E/E_c \simeq 1$), and $E_f/h = 216$ Hz ($E/E_c \simeq 0.8$), revealing the three characteristic long-time scaling laws (18) across the mobility edge. Points are the results of numerical simulations and solid lines show the predictions of the SCT. Dashed lines are guides indicating the algebraic laws expected at long time. Here numerical results are averaged over 48 disorder realizations, and we fit $(\alpha_0, \beta) \simeq (10.7 \text{ s}^{-1/3}, 4.6 \mu\text{m}\cdot\text{s}^{-1/3})$ for the SCT parameters.

To compare the numerical results of Fig. 3 with the SCT, we start from the narrow-filter approximation (11) applied to the linear density,

$$n_{1d}(z, t) \simeq \int_{-\infty}^{\infty} dz' P_E(z, z', t) n_{1d}(z', t = 0), \quad (19)$$

where $n_{1d}(z', t = 0) \equiv \int dx' dy' |\phi(x', y', z')|^2$. The 1D propagator is deduced from Eq. (12):

$$\begin{aligned} P_E(z, z', t) &= \int_{-\infty}^{\infty} \frac{d\omega}{2\pi} \int_{-\infty}^{\infty} \frac{dq_z}{2\pi} \frac{e^{iq_z(z-z')-i\omega t}}{-i\omega + D(\omega)q_z^2} \\ &= \int_{-\infty}^{\infty} \frac{d\omega}{2\pi} \frac{e^{-i\omega t}}{\sqrt{-4i\omega D(\omega)}} \exp\left[-|z-z'| \sqrt{\frac{-i\omega}{D(\omega)}}\right], \end{aligned} \quad (20)$$

with the diffusion coefficient $D(\omega)$ determined from Eq. (15). Note that the propagator is normalized, $\int dx P_E(z, z', t) = 1$, and so is the linear density $n_{1d}(z, t)$. Because the profiles represented in Fig. 3 typically correspond to times well beyond to the mean free time τ^1 ,

¹From [51], we estimate a scattering mean free time $\tau \simeq 1$ ms for a speckle disorder with the properties of Fig. 2.

Eq. (20) can be further simplified by using the small-frequency asymptotic relations (16) for $D(\omega)$. In the diffusive regime $E > E_c$, they lead to the well-known Gaussian distribution

$$P_{E>E_c}(z, z', t) = \frac{1}{\sqrt{4\pi Dt}} \exp\left(-\frac{|z - z'|^2}{4Dt}\right) \quad (21)$$

where $D = 3\beta^2\alpha_0(E/E_c - 1)$, while in the localized regime $E < E_c$ one has

$$P_{E<E_c}(z, z', t) = \frac{1}{2\xi} \exp\left(-\frac{|z - z'|}{\xi}\right) \quad (22)$$

where $\xi = 2\beta/[3\alpha_0(1 - E/E_c)]$. At the mobility edge $E = E_c$, finally, the linear density is an Airy function [59, 60]:

$$P_{E=E_c}(z, z', t) = \frac{3\sqrt{\varrho}}{2(3t)^{1/3}} \text{Airy}\left[\frac{\sqrt{\varrho}|z - z'|}{(3t)^{1/3}}\right] \quad (23)$$

with $\varrho = 4^{1/3}\beta^2$.

Figure 3a-c shows as solid curves the SCT prediction (19) for the linear density, using the asymptotic expressions (21), (22) and (23). For the comparison, we use a Gaussian initial profile as in the simulations, $n_{1d}(z, t=0) = \exp(-z^2/2\Delta z^2)/\sqrt{2\pi\Delta z^2}$, with $\Delta z \simeq 4.6 \mu\text{m}$ determined from a fit of the numerical profiles immediately after loading into the disorder², and take α_0 and β as fit parameters. The value of $\beta = 4.6 \mu\text{m}\cdot\text{s}^{-1/3}$ is first obtained by fitting the profiles at the mobility edge using Eq. (23), which does not depend on α_0 . The parameter $\alpha_0 = 10.7 \text{s}^{-1/3}$ is subsequently extracted by fitting the central density $n_{1d}(z=0, t)$ as a function of the target energy $E = E_f$ (not shown).

Overall, Fig. 3a-c shows very good agreement between the SCT and the *ab initio* simulations over the range of times and energies explored (typically $E_f = E_c \pm 0.2E_c$, for evolution times up to 7 s). In particular, the tails of the density profiles are very well reproduced by the theory, both in the localized regime and at the critical point—an encouraging result given the approximate nature of the SCT. Note that despite the relatively narrow initial Gaussian distribution, the density profiles remain close to the initial shape in the localized regime for the chosen disorder amplitude. This behavior is also observed experimentally (see Sec. 4).

In the diffusive regime, by contrast, we observe significant deviations between theory and simulations in the tails. These discrepancies originate from the finite size L of the numerical domain, which starts to affect the profiles once the wave packet reaches the domain boundaries. This interpretation is supported by theory: replacing the unbounded expression (21) with the diffusive solution in a finite box of size L (with periodic boundary conditions, as in the simulations), we find [47]

$$n_{1d}(z, t) = \frac{1}{L} \left[1 + 2 \sum_{n=1}^{\infty} \cos\left(\frac{2\pi n z}{L}\right) \exp\left[-\left(Dt + \frac{\Delta z^2}{2}\right)\left(\frac{2\pi n}{L}\right)^2\right] \right], \quad (24)$$

which yields an excellent agreement with the simulations, including in the tails (see Fig. 3a).

Figure 3d finally shows the inverse central density of the wave packet, $n_{1d}^{-1}(z=0, t)$, as a function of time for three target energies in the diffusive, localized, and critical regimes. The plot reveals the three characteristic long-time scaling laws (18) for the packet width, $\sqrt{\langle \mathbf{r}^2(t) \rangle} \propto \sqrt{\langle z^2(t) \rangle} \propto n_{1d}^{-1}(0, t)$, with again very good agreement between the SCT and the *ab initio* simulations. This analysis confirms that the theoretical framework reliably captures the dynamics across the mobility edge, even in a regime of relatively strong disorder, large spatial scales, and long times, where direct numerical simulations become highly demanding.

4 Theory versus experiments

We now present comparisons between the SCT and the experimental observation of the density-profile dynamics obtained with the setup of Ref. [40]. We begin with a brief

²In the derivation of Eq. (19), it is assumed that the BEC profile $|\phi(\mathbf{r})|^2$ in state |1⟩ remains unchanged by the rf transfer. Although we have verified numerically that this assumption holds to a good approximation, a slightly more accurate comparison is obtained by using in Eq. (19) the post-transfer profile, of size $\Delta z \simeq 4.6 \mu\text{m}$, which is slightly larger than $\Delta r = 3.5 \mu\text{m}$.

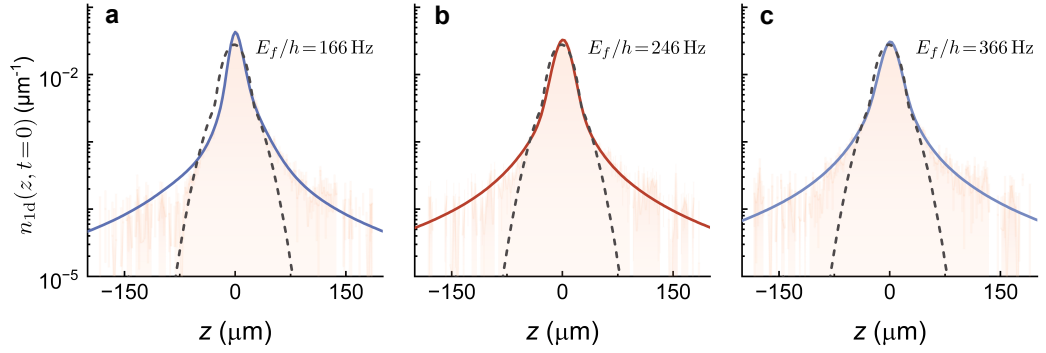


Figure 4. Initial one-dimensional density profiles of atoms in state $|2\rangle$ immediately after transfer along the z axis, $n_{1d}(z, t=0)$. The shaded orange areas show the experimental profiles on a semi-log scale for three target energies: (a) $E_f/h = 166$, (b) 246, and (c) 366 Hz. Dashed curves indicate, for comparison, the time-of-flight estimate of the BEC density profile in state $|1\rangle$ before the rf transfer, including the thermal component. Both profiles are normalized to unit integral for proper comparison. Solid curves are fits of $n_{1d}(z, t=0)$ to pseudo-Voigt profiles, which are used as input for the SCT.

description of the experimental conditions (Sec. 4.1) and of the corresponding initial density profiles, which serve as the input to the SCT. We then characterize the atomic energy distribution realized in the experiment, accounting for the residual thermal background cloud (Sec. 4.2). Finally, we provide a quantitative comparison between the measured density profiles and the theoretical predictions over a range of target energies spanning the mobility edge.

4.1 Energy-resolved state preparation

The crucial feature of the experiments reported in Ref. [40] is the energy-resolved state preparation, as sketched in Fig. 1. The sequence starts with the preparation of a ^{87}Rb BEC in state $|1\rangle = |F=2, m_F=1\rangle$, containing $\sim 2 \times 10^5$ atoms in a nearly isotropic optical trap with frequencies $(\omega_x, \omega_y, \omega_z) \approx 2\pi \times (35, 25, 11)$ Hz. The temperature is $T \simeq 7$ nK and the condensate fraction is around $f_c \simeq 75\%$. The BEC is characterized by the chemical potential $\mu_{\text{in}}/h \simeq 350$ Hz, yielding the Thomas–Fermi radii $R_{\text{TF}} \simeq (8, 12, 26)$ μm .

The state-dependent disorder is created using a bichromatic optical speckle, following the principle described in Ref. [42]. A small fraction of atoms ($\sim 5\%$) is then transferred to the state $|2\rangle = |F=1, m_F=-1\rangle$ by applying a radio-frequency (rf) pulse. The rf frequency sets the target energy to $E_f = \hbar\delta_{\text{rf}}$, where δ_{rf} is the detuning from the bare resonance in absence of disorder (see Fig. 1). The rf pulse duration, $t_{\text{rf}} \simeq 40$ ms, defines the energy width $\Delta E \sim \hbar/t_{\text{rf}}$ of the energy-resolved wave packet (see below). Immediately after the transfer, at $t=0$, the optical trap is switched off and the remaining atoms in state $|1\rangle$ are removed. The subsequent evolution of the wave packet in the disordered potential is then monitored up to 5 seconds by *in-situ* fluorescence imaging along the x axis. During the whole experimental sequence, the atoms are suspended against gravity using a magnetic levitation scheme. Such levitation yields a shallow residual harmonic confinement³ in the horizontal plane x - y , such that the expansion occurs essentially along the vertical z axis. Following the analysis done in Ref. [40], we then integrate further the recorded column density $n_{\text{col}}(y, z, t) = \int dx n_{\text{exp}}(\mathbf{r}, t)$, and we study the one-dimensional profile $n_{1d}(z, t) = \int dy n_{\text{col}}(y, z, t)$ along z .

For each energy E_f , we record the initial profile $n_{1d}(z, t=0)$ immediately after transfer. Examples are shown in Fig. 4 for $E_f/h = 166, 246$ and 366 Hz (solid curves with orange shading). The dashed lines indicate the estimated initial density profile of the BEC in state $|1\rangle$ before transfer, including the thermal component. Weak tails are visible in $n_{1d}(z, t=0)$. We attribute them to a combination of short-time interaction effects, and possible dynamics in state $|2\rangle$ during the rf coupling stage.

³Although the precise influence of the weak confinement remains to be precisely investigated, the transport dynamics remains fully 3D since the transverse size of the cloud is much larger than the expected scattering mean path $\ell \simeq 1$ μm , see Ref. [40].

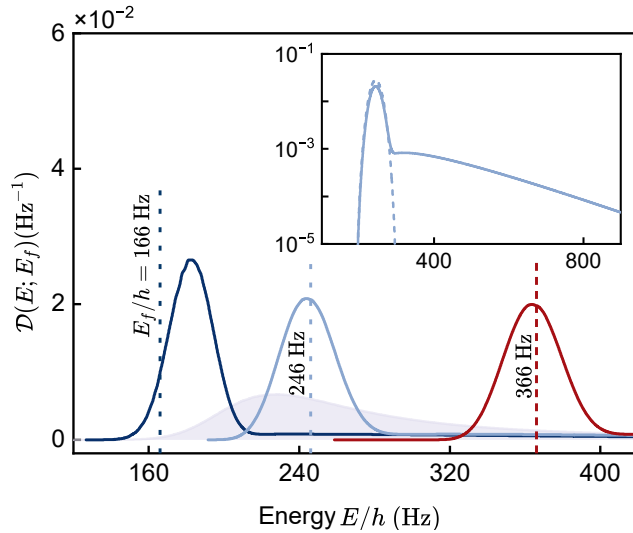


Figure 5. Estimated energy distribution $\mathcal{D}(E; E_f)$ of the atoms experimentally transferred into a random potential of amplitude $V_R/h = 416$ Hz, for three target energies $E_f/h = 166$ (left), 246 (middle), and 366 Hz (right), indicated by vertical dashed lines. The distributions $\mathcal{D}(E; E_f)$ are calculated using Eq. (25), assuming a thermal fraction of 25% in state $|1\rangle$. Each distribution consists of a dominant BEC component, numerically computed from Eq. (25), superimposed on a small, smooth thermal background [Eq. (26)], which exhibits a long tail toward higher energies. The inset displays the distribution for $E_f/h = 246$ Hz on a semi-logarithmic scale, highlighting the high-energy thermal tail; the dashed line shows the result obtained for a pure BEC in state $|1\rangle$ ($f_c = 1$). In the main panel, the shaded area shows the spectral function $A(E, \mathbf{k} = 0)$, whose numerical computation is detailed in Appendix C.4.

4.2 Energy distribution

The key objective of the rf transfer scheme is to prepare an atomic cloud with a narrow energy distribution in state $|2\rangle$. In the weak-coupling regime in which the experiment operates [40], the energy spread of the transferred atoms is Fourier-limited, $\Delta E \sim h/t_{\text{rf}}$. In this case, and assuming that the atoms in state $|1\rangle$ form a pure BEC, the transferred state $|\psi_0^{\text{exp}}\rangle$ is also pure and has an energy distribution $\mathcal{D}_{\text{BEC}}(E; E_f) = F(E - E_f) A(E, \mathbf{k} = 0)$ given by Eq. (1). The filter function $F(E)$ is determined by the Fourier transform of the temporal envelope of the rf pulse, which has the shape of a Kaiser function [40]. This leads to a narrow rms energy width $\Delta E/h \simeq 14$ Hz.

In the experiment, however, the initial atomic cloud in state $|1\rangle$ is not a fully pure BEC but it contains a finite thermal fraction, $1 - f_c \simeq 25\%$. This thermal component gives rise to an additional contribution \mathcal{D}_{th} in the energy distribution, which generalizes to:

$$\mathcal{D}(E; E_f) = f_c \mathcal{D}_{\text{BEC}}(E; E_f) + (1 - f_c) \mathcal{D}_{\text{th}}(E; E_f), \quad (25)$$

where (see Appendix B)

$$\mathcal{D}_{\text{th}}(E; E_f) \simeq \frac{2(k_B T)^{-3/2}}{\sqrt{\pi}} \Theta(E - E_f) \sqrt{E - E_f} \exp\left(-\frac{E - E_f}{k_B T}\right). \quad (26)$$

The thermal contribution describes the rf transfer into the disorder of the thermal atoms initially present in state $|1\rangle$. As shown in Appendix B, it generally involves a convolution of the energy filter $F(E)$ with the Boltzmann factor $\exp(-E/k_B T)$. However, owing to the relatively large thermal scale $k_B T/h \sim 140$ Hz at $T = 7$ nK, the resulting distribution $\mathcal{D}_{\text{th}}(E; E_f)$ essentially reduces—up to a prefactor given by the density of states $\rho(E) \propto \sqrt{E}$ —to the Boltzmann weight $\exp[-(E - E_f)/k_B T]$.

Figure 5 shows energy distributions $\mathcal{D}(E; E_f)$ calculated numerically from Eq. (25) for three target energies, $E_f/h = 166$, 246 and 366 Hz (indicated by vertical dashed lines), for a disorder amplitude of $V_R/h = 416$ Hz and a thermal fraction $1 - f_c = 0.25$. The shaded area represents the zero-momentum spectral function $A(E, \mathbf{k} = 0)$ that is used to calculate the energy distribution from Eq. (1) (see Appendix C.4 for details on the numerical computation of the spectral function). Although the thermal contribution yields a broad pedestal (see inset of Fig. 5), it remains small enough such that the energy distribution remains essentially very narrow, one [31, 32] or even two [30, 33] orders of magnitude smaller than in previous experiments.

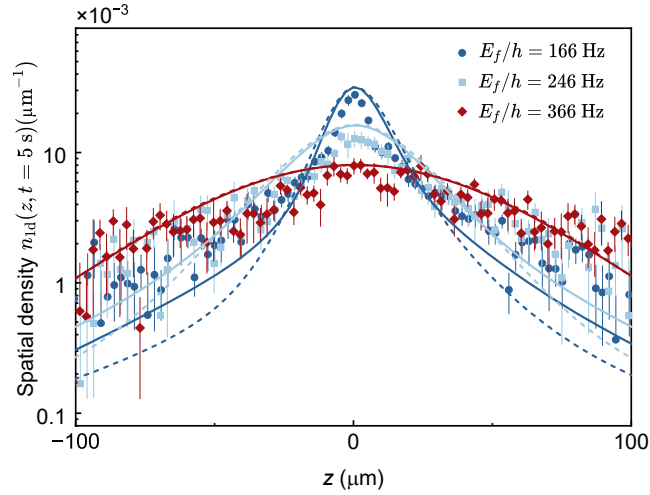


Figure 6. 1D density profiles $n_{1d}(z, t)$, after an expansion of $t = 5$ s in the disorder, for three energies: $E_f/h = 166, 246,$ and 366 Hz. Symbols are the experimentally measured profiles, while solid lines show the corresponding SCT predictions ($\alpha_0 = 4.29 \text{ s}^{-1/3}$, $\beta = 2.97 \mu\text{m} \text{ s}^{-1/3}$). The pronounced differences between the profiles illustrate the Anderson transition as E_f crosses the mobility edge ($E_c^{\text{exp}}/h \simeq 237$ Hz from Ref. [40]). The dashed curves show for comparison the prediction of the SCT assuming a pure BEC in state $|1\rangle$ ($f_c = 1$ instead of $f_c = 0.75$), demonstrating the importance of properly accounting for the atomic energy distribution given by Eq. (25).

4.3 Comparison with 3D self-consistent theory

Knowing both the initial density profile and the energy distribution $\mathcal{D}(E; E_f)$ from Eq. (25), we have all the ingredients required to compute the 1D integrated density profile at any times. From Eq. (9), it is given by

$$n_{1d}(z, t) = \int_{-\infty}^{\infty} dz' \int_0^{\infty} dE \mathcal{D}(E; E_f) P_E(z, z', t) n_{1d}(z', t = 0), \quad (27)$$

where P_E is the disorder-averaged propagator defined in Eq. (20). For the computation, the initial profile $n_{1d}(z', t = 0)$ is obtained by fitting the experimental density distribution measured immediately after the rf transfer. To account for the slight asymmetry observed in these profiles, we employ an asymmetric pseudo-Voigt fitting function (see Ref. [61]).

Examples of these fits are shown as solid lines in Fig. 4.

As explained in Sec. 2.4, the self-consistent theory depends on three effective parameters: the mobility edge E_c , and the coefficients α_0 and β . Here the mobility edge is fixed independently using the experimental determination $E_c^{\text{exp}}/h \simeq 237$ Hz reported in Ref. [40] (and in agreement with transfer-matrix computations [23]). The remaining parameters, α_0 and β , are calibrated from a global comparison between the SCT and the experimental dynamics. To this end, we use the central density $n(z = 0, t)$ as the fitting observable. This choice is physically motivated by the fact that the central density is less noisy than, for example, the tails of the profiles (which are affected by finite signal-to-noise), while still fully capturing the dynamics of the cloud expansion. The parameters α_0 and β are determined by minimizing the least-squares cost function

$$\chi^2(\alpha_0, \beta) = \sum_{E_f} \sum_t [n_{\text{exp}}(0, t)|_{E_f} - n_{\text{SCT}}(0, t)|_{E_f, \alpha_0, \beta}]^2, \quad (28)$$

where $n_{\text{exp}}(0, t)|_{E_f}$ denotes the measured central density at energy E_f , and $n_{\text{SCT}}(0, t)|_{E_f, \alpha_0, \beta}$ is the corresponding SCT prediction for a given parameter pair (α_0, β) . The double sum runs over target energies spanning the mobility edge and over evolution times up to three seconds. This procedure is applied both to the ideal energy distribution $\mathcal{D}_{\text{BEC}}(E; E_f)$ —corresponding to a pure BEC in state $|1\rangle$ —and to the full distribution $\mathcal{D}(E; E_f)$ that accounts for the 25% thermal fraction [see Eq. (25)].

We first show in Fig. 6 the experimental density profiles $n_{1d}(z, t)$ of atoms in state $|2\rangle$ along the z -axis at the maximum evolution time $t = 5$ s, for the three energies $E_f/h = 166,$

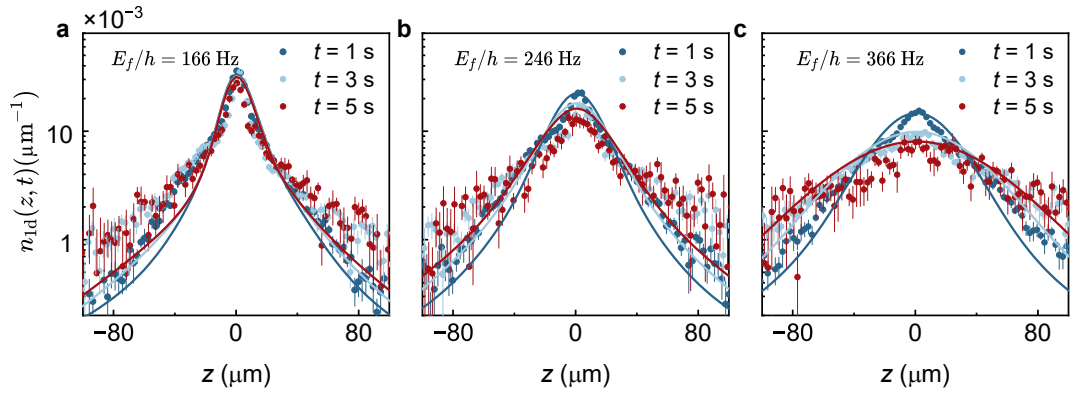


Figure 7. Time evolution of the 1D density profiles $n_{1d}(z, t)$ in the disorder amplitude $V_R/h = 416$ Hz for three target energies: (a) $E_f/h = 166$, (b) 246, and (c) 366 Hz. Symbols denote experimental data at $t = 1, 3,$ and 5 s (semi-log scale). Solid lines represent the results of the SCT taking into account the thermal fraction $1 - f_c = 0.25$ in the energy distribution. The evolution of the profiles with energy and time reflects the transition from the diffusive to the localized regime. Each point is averaged over 6–9 independent experimental runs, and error bars indicate the standard error of the mean.

246 and 366 Hz considered so far. The pronounced change in the profile shapes illustrates the expected behavior across the mobility edge $E_c^{\text{exp}} \simeq 237$ Hz: from a sharply peaked profile with exponentially decaying tails in the localized regime, to a broad profile in the diffusive regime. The experimental data are compared with the theoretical prediction (27) using either $\mathcal{D}_{\text{BEC}}(E; E_f)$ ($f_c = 1$, dashed curves) or $\mathcal{D}(E; E_f)$ (with $f_c = 0.75$, solid curves) for the energy distribution. In the diffusive regime, both choices provide a good description of the data. However, at the mobility edge and in the localized regime, significantly better agreement – particularly in the tails of the density profiles – is obtained when the thermal fraction is properly taken into account. This confirms the crucial role of the atomic energy distribution and highlights the need for an accurate characterization of the initial cloud in order to reproduce the observed spatial profiles (see also Refs. [31, 62, 32, 33]).

We note that even when thermal atoms are included, a residual discrepancy remains in the density tails in the localized regime. This may originate from effects present in the experiment but not included in the theory, such as interactions during the rf transfer or the residual shallow harmonic confinement in the x - y plane. These mechanisms may also account for the values $\alpha_0 = 4.29 \text{ s}^{-1/3}$ and $\beta = 2.97 \mu\text{m s}^{-1/3}$, which are slightly smaller – though of the same order of magnitude – than those obtained under ideal conditions in the numerical simulations of Sec. 3.

We further show in Fig. 7 the time evolution of 1D density profiles $n_{1d}(z, t)$ for the same three energies (points, experimental data), together with the prediction of the SCT taking into account the finite thermal fraction of the cloud (solid curves). The plots clearly reveal atomic spreading in the diffusive regime, while the profiles remain nearly time-independent in the localized regime. Fig. 7a also suggests that, in the localized regime, the core of the distribution appears slightly narrower than the initial density profile shown in Fig. 4. We tentatively attribute this feature to the intrinsically strong spatial fluctuations of the localized eigenstates onto which the density profile decomposes. In the experiment, the averaging over disorder realizations is only partial, so that residual signatures of these fluctuations may persist in the measured profiles. Such effect lies beyond the scope of the SCT, which essentially provides a mean-field description of the Anderson transition, but would be worthwhile to investigate in future work.

5 Conclusion

In this work, we have developed a flexible theoretical framework for quantitatively describing the dynamics of matter-wave packets in three-dimensional random potentials. The approach combines an accurate characterization of the atomic energy distribution with a three-dimensional implementation of the self-consistent theory of localization, providing access to the dynamics across the mobility edge. Although the SCT is intrinsically approximate, we have shown that it accurately reproduces exact 3D numerical simulations in a nontrivial anisotropic speckle potential, while being significantly less computationally demanding.

Within this framework, we have further achieved quantitative agreement with the density profiles reported in the recent experiment of Ref. [40], where the dynamics near the Anderson transition could be probed using well-controlled atomic energy distributions.

Beyond the present study, our methodology can be readily extended to other platforms, such as fermionic systems [30, 33]. It would also be interesting to generalize the approach to more complex scenarios, for instance by including a shallow transverse confinement, as in the experiment of Ref. [40], or by incorporating weak atom–atom interactions within the SCT, following the lines of previous works [63, 46].

On the experimental side, it would be highly appealing to apply the rf-transfer scheme to other physical problems. Relevant examples include measurements of critical exponents or multifractality [60, 64, 65], investigations of percolation transitions in random potentials [66] and their connection to Anderson physics [26], exploration of localization phenomena in momentum space [17, 67, 68], and characterization of mobility edges and critical phases in one-dimensional quasi-periodic potentials [69, 70, 71, 72].

A Disorder-average density

In this appendix, we provide details on the derivation of the disorder-average density, Eq. (9). Our starting point is the general relation (8), in which we express the Green's function correlator in the hydrodynamic regime as [47]

$$\overline{G^R(\mathbf{r}, \mathbf{r}', E_+)G^A(\mathbf{r}'', \mathbf{r}, E_-)} \simeq \frac{1}{2\pi\rho\tau^2} \int d\mathbf{r}_1 d\mathbf{r}_2 |\overline{G^R}(\mathbf{r}, \mathbf{r}_2, E)|^2 P_E(\mathbf{r}_1, \mathbf{r}_2, \omega) \times \overline{G^R}(\mathbf{r}_1, \mathbf{r}', E) \overline{G^{R*}}(\mathbf{r}_1, \mathbf{r}'', E). \quad (29)$$

Here $\overline{G^R}$ [$\overline{G^A}$] is the averaged retarded (advanced) Green's function, $P_E(\mathbf{r}_1, \mathbf{r}_2, \omega)$ is the quantum propagator, which gives the probability density for an atom of energy E to propagate from \mathbf{r}_1 to \mathbf{r}_2 , τ is the scattering mean free path and ρ the density of states per unit volume. Next, we insert this decomposition into Eq. (8) and introduce the Wigner change of variables $(\mathbf{r}', \mathbf{r}'') \rightarrow [\mathbf{R} = (\mathbf{r}' + \mathbf{r}'')/2, \Delta\mathbf{r} = \mathbf{r}' - \mathbf{r}'']$. This leads to

$$|\overline{\psi}(\mathbf{r}, t)|^2 = \int \frac{dE}{2\pi} \frac{d\omega}{2\pi} e^{-i\omega t} \int d\mathbf{R} d\Delta\mathbf{r} d\mathbf{r}_1 d\mathbf{r}_2 \overline{G^R}(\mathbf{r}_1, \mathbf{R} + \Delta\mathbf{r}/2, E) \overline{G^{R*}}(\mathbf{r}_1, \mathbf{R} - \Delta\mathbf{r}/2, E) \times \frac{1}{2\pi\rho\tau^2} P(\mathbf{r}_1, \mathbf{r}_2, \omega) |\overline{G^R}(\mathbf{r}, \mathbf{r}_2, E)|^2 |f(E - E_f)|^2 \phi(\mathbf{R} + \Delta\mathbf{r}/2) \phi^*(\mathbf{R} - \Delta\mathbf{r}/2). \quad (30)$$

To simplify this expression, we proceed in two steps. First, instead of directly working with the product $\phi\phi^*$ of initial wave functions in real space, it is convenient to introduce the *Wigner distribution* $W(\mathbf{R}, \mathbf{k})$ of the initial state, defined by the relation:

$$\phi(\mathbf{R} + \Delta\mathbf{r}/2) \phi^*(\mathbf{R} - \Delta\mathbf{r}/2) = \int \frac{d\mathbf{k}}{(2\pi)^3} e^{i\mathbf{k}\cdot\Delta\mathbf{r}} W(\mathbf{R}, \mathbf{k}). \quad (31)$$

The main interest of the Wigner distribution is to simultaneously encode the spatial *and* momentum structures of the initial state. In particular, it gives access to the spatial density after integration over the momentum variable:

$$\int \frac{d\mathbf{k}}{(2\pi)^3} W(\mathbf{R}, \mathbf{k}) = \overline{|\phi(\mathbf{r})|^2}. \quad (32)$$

Second, we use that at scales larger than the mean free path (hydrodynamic regime), $P(\mathbf{r}_1, \mathbf{r}_2, \omega)$ is a smooth function of \mathbf{r}_1 and \mathbf{r}_2 , so that $P(\mathbf{r}_1, \mathbf{r}_2, \omega) \simeq P(\mathbf{R}, \mathbf{r}, \omega)$. With this simplification, the three integrals over $\Delta\mathbf{r}$, \mathbf{r}_1 and \mathbf{r}_2 in Eq. (30) can be easily performed, yielding:

$$|\overline{\psi}(\mathbf{r}, t)|^2 \simeq \frac{1}{\tau} \int \frac{dE}{2\pi} \int d\mathbf{R} \int \frac{d\mathbf{k}}{(2\pi)^3} |\overline{G^R}(\mathbf{k}, E)|^2 |f(E - E_f)|^2 P_E(\mathbf{R}, \mathbf{r}, t) W(\mathbf{R}, \mathbf{k}). \quad (33)$$

In the last step, we note that the momentum width of $|\overline{G^R}(\mathbf{k}, E)|^2$ is of order $1/\ell$, where ℓ is the scattering mean free path, whereas the Wigner distribution has a momentum width $\sim 1/R_0$, with R_0 the spatial extent of the initial wave packet. In the experiment [40], one typically has $R_0 \gg \ell$, so that in Eq. (33) one can approximate $|\overline{G^R}(\mathbf{k}, E)|^2 \simeq |\overline{G^R}(\mathbf{k} = 0, E)|^2$. This enables us to perform the integral over \mathbf{k} using Eq. (32). Noting further that $|\overline{G^R}(0, E)|^2 \equiv 2\pi\tau A(E, \mathbf{k} = 0)$, where A is the spectral function, we recover Eq. (9) of the main text.

B Energy distribution of the atomic cloud

In this appendix, we present a derivation of the energy distribution (25), which accounts for a finite thermal contribution given by Eq. (26). The starting point is the density matrix of the Bose gas in state $|1\rangle$ prior to transfer:

$$\hat{\rho} = f_c |\mathbf{k} = 0\rangle \langle \mathbf{k} = 0| + (1 - f_c) \frac{e^{-\hat{H}_0/k_B T}}{Z}, \quad (34)$$

where \hat{H}_0 is the free-space Hamiltonian, Z a normalization factor, and we have approximated $|\phi\rangle \simeq |\mathbf{k} = 0\rangle$ for the BEC wave function. The rf pulse transfers an initial energy E_1 in state $|1\rangle$ to a final energy $E_2 = E_1 + \hbar\omega_{\text{rf}}$ in the disorder-sensitive state $|2\rangle$. For an initial $|\mathbf{k}\rangle$ state, $E_1 = E_k \equiv \hbar^2 \mathbf{k}^2 / (2m)$, and the transfer in the disorder corresponds to the transformation $|\mathbf{k}\rangle \rightarrow f(\hat{H} - E_k - E_f)|\mathbf{k}\rangle$, which generalizes Eq. (2), with $E_f \equiv \hbar\omega_{\text{rf}}$ the transferred energy. The energy distribution in the disorder after transfer is defined as

$$\mathcal{D}(E) \equiv \text{Tr} \left[\overline{\hat{\rho} \delta(E - \hat{H})} \right]. \quad (35)$$

The initial BEC state $|\mathbf{k} = 0\rangle$ has energy $E_1 = 0$, so its energy distribution after transfer in the disorder reads

$$\mathcal{D}_{\text{BEC}}(E) = f_c \langle \mathbf{k} = 0 | f^*(\hat{H} - E_f) \overline{\delta(E - \hat{H})} f(\hat{H} - E_f) | \mathbf{k} = 0 \rangle, \quad (36)$$

which immediately leads to Eq. (1) of the main text.

Consider now the energy distribution of the thermal component. Since the thermal factor $e^{-\hat{H}_0/k_B T}$ in Eq. (34) involves the free Hamiltonian, it is convenient to introduce the basis states $\{E_k, |\mathbf{k}\rangle\}$ to evaluate the trace:

$$\begin{aligned} \mathcal{D}_{\text{Th}}(E) &= \frac{1 - f_c}{Z} \int \frac{d\mathbf{k}}{(2\pi)^3} \overline{\langle \mathbf{k} | f^*(\hat{H} - E_k - E_f) e^{-\hat{H}_0/k_B T} \delta(E - \hat{H}) f(\hat{H} - E_k - E_f) | \mathbf{k} \rangle} \\ &= \frac{1 - f_c}{Z} \int \frac{d\mathbf{k}}{(2\pi)^3} F(E - E_k - E_f) e^{-E_k/k_B T} A(E, \mathbf{k}). \end{aligned} \quad (37)$$

We then approximate $A(E, \mathbf{k}) \simeq A(E - E_k, \mathbf{k} = 0)$, and change variable in the momentum integral from \mathbf{k} to $E' = \hbar^2 \mathbf{k}^2 / (2m)$. This leads to:

$$\mathcal{D}_{\text{Th}}(E) = \frac{1 - f_c}{Z} \int dE' \rho(E') F(E - E' - E_f) e^{-E'/k_B T} A(E - E', \mathbf{k} = 0), \quad (38)$$

with ρ the free-space density of states in three dimensions. We finally perform the integral over E' using that the filter function is much narrower than the spectral function, the thermal factor and the density of states:

$$\mathcal{D}_{\text{Th}}(E) \simeq \frac{1 - f_c}{Z} \rho(E - E_f) A(E_f, \mathbf{k} = 0) e^{-(E - E_f)/k_B T}. \quad (39)$$

Using that $\rho(x) = \Theta(x) \sqrt{x}$ in three dimensions (with Θ the Heaviside step function), and imposing the normalizing condition $\int dE \mathcal{D}_{\text{th}}(E) = 1 - f_c$, we finally obtain Eqs. (26) of the main text.

C Numerical methods

C.1 Numerical generation of the speckle potential

Experimentally, the speckle potential is generated by illuminating a diffusive lens with a laser beam of vacuum wavelength $\lambda = 780$ nm (wavenumber $k_L = 2\pi/\lambda = 8.06 \mu\text{m}^{-1}$). The incident beam is Gaussian, with a waist of $w = 9.9$ mm at the lens plane, and is truncated by a diaphragm of diameter $D = 20.4$ mm. The lens has a focal length $d = 15.2$ mm. The beam propagates along the x -axis and is linearly polarized in the (y, z) -plane. Numerically, the speckle potential is computed using a Fourier-filtering method similar to that in Ref. [41]. The electric field along the polarization direction is expressed in the Fourier representation as

$$E(\mathbf{r}) = E_0 \int_{k_x > 0} \frac{d\mathbf{k}}{(2\pi)^3} \xi(\mathbf{k}) \exp\left(-\frac{k_{\parallel}^2 d^2}{k_L^2 w^2}\right) \Theta(k_c - k_{\parallel}) \delta(k^2 - k_L^2) \exp(i\mathbf{r} \cdot \mathbf{k}). \quad (40)$$

Here, E_0 is an arbitrary amplitude, and ξ is a uncorrelated, complex Gaussian stationary stochastic process with zero mean. The wave vector $\mathbf{k}_\parallel = (k_y, k_z)$ denotes the projection of \mathbf{k} onto the (y, z) -plane, and $k_c = k_L[(D/2d)^2/(1 + (D/2d)^2)]^{1/2}$ is the cutoff set by the diaphragm. The Dirac distribution $\delta(k^2 - k_L^2)$ enforces the light's dispersion relation in vacuum. Numerically, the integral (40) is evaluated using a 3D fast Fourier transform on a rectangular grid, approximating the Dirac distribution by a narrow Gaussian of width Δk : $\delta(|\mathbf{k}|^2 - k_L^2) \approx \exp[-(k^2 - k_L^2)^2/(2\Delta k^2)]/(\sqrt{2\pi}\Delta k)$.

Equation (40) implies that the field is a sum of independent Gaussian random variables $\xi(\mathbf{k})$. Consequently, the probability density of the potential $V(\mathbf{r}) = K|E(\mathbf{r})|^2$, where K is a constant characterizing the light-atom interaction, follows the exponential distribution $P(V) = \exp(-V/V_R)/V_R \cdot \Theta(V)$ [73]. The average potential V_R is obtained from $V_R = K\overline{|E(\mathbf{r})|^2}$, using the uncorrelated nature of ξ : $\xi(\mathbf{k})\xi^*(\mathbf{k}') = (2\pi)^3\delta(\mathbf{k} - \mathbf{k}')$. This yields $V_R = K|E_0|^2\mathcal{I}$, where

$$\mathcal{I} = \int \frac{d\mathbf{k}}{(2\pi)^3} \exp\left(-\frac{2k_\parallel^2 d^2}{k_L^2 w^2}\right) \Theta(k_c - k_\parallel) \delta(k^2 - k_L^2). \quad (41)$$

To numerically generate the speckle potential shown in Fig. 2a–b, we proceed as follows. We evaluate Eq. (40) with $E_0 = 1$ using a numerically generated random noise ξ (the corresponding numerical parameters are given in Sec. 3.1). The resulting field is normalized by \mathcal{I} , and the potential is then obtained as $V(\mathbf{r}) = V_R|E(\mathbf{r})|^2/\mathcal{I}$, where $V_R = 416$ Hz is the experimental rms disorder strength.

From the numerically generated speckle potential, the autocorrelation function shown in Fig. 2c is computed as $C(\Delta\mathbf{r}) = \overline{V(\mathbf{r})V(\mathbf{r} + \Delta\mathbf{r})}/V_R^2 - 1$. In the same figure, this result is compared with the theoretical prediction, which follows directly from Eq. (40) using the Gaussian character of ξ :

$$C(\Delta\mathbf{r}) = \frac{1}{\mathcal{I}^2} \left| \int \frac{d\mathbf{k}}{(2\pi)^3} \exp\left(-\frac{2k_\parallel^2 d^2}{k_L^2 w^2}\right) \Theta(k_c - k_\parallel) \delta(k^2 - k_L^2) \exp(i\mathbf{k} \cdot \Delta\mathbf{r}) \right|^2. \quad (42)$$

C.2 Chebyshev polynomial expansion of operators

The numerical computation of the initial energy-resolved state, the spectral function, and the time evolution of the wave packet presented in the main text relies on a unified framework based on Chebyshev polynomial expansions of operator functions of the Hamiltonian. The calculations are performed on the spatial grid used to generate the speckle potential, with the Laplacian term of the Hamiltonian discretized using a three-point finite-difference stencil in each spatial direction.

In the three cases, the problem reduces to applying a given operator function of the Hamiltonian, $\mathcal{F}(\hat{H})$, to an initial state. Since full diagonalization of the 3D Hamiltonian would be computationally prohibitive, we approximate $\mathcal{F}(\hat{H})$ by a truncated Chebyshev expansion. To this end, the discrete Hamiltonian is first shifted and rescaled so that its spectrum lies in the interval $(-1, 1)$, where Chebyshev polynomials are defined. Given bounds E_{\min} and E_{\max} of the spectrum, we define $E_{\text{mid}} = (E_{\max} + E_{\min})/2$ and introduce the rescaled operator $\tilde{H} = 2(\hat{H} - E_{\text{mid}})/(E_{\max} - E_{\min})$, whose eigenvalues lie in $(-1, 1)$. Using

$$\mathcal{F}(\tilde{H}) = \int_{-1}^1 \delta(\varepsilon - \tilde{H}) \mathcal{F}(\varepsilon) d\varepsilon, \quad (43)$$

together with the Chebyshev expansion for the Dirac distribution [74],

$$\delta(\varepsilon - \tilde{H}) = \frac{1}{\pi\sqrt{1 - \varepsilon^2}} \left[T_0(\tilde{H}) + 2 \sum_{n=1}^{\infty} T_n(\tilde{H}) T_n(\varepsilon) \right], \quad (44)$$

one obtains the Chebyshev expansion

$$\mathcal{F}(\tilde{H}) = c_0 T_0(\tilde{H}) + 2 \sum_{n=1}^{\infty} c_n T_n(\tilde{H}), \quad c_n = \int_{-1}^1 \frac{\mathcal{F}(\varepsilon) T_n(\varepsilon)}{\pi\sqrt{1 - \varepsilon^2}} d\varepsilon, \quad (45)$$

where T_n denotes the Chebyshev polynomial of the first kind of order n . Applying $\mathcal{F}(\tilde{H})$ to a state $|\phi\rangle$ thus amounts to computing the vectors $|n\rangle = T_n(\tilde{H})|\phi\rangle$, generated recursively via

$$|0\rangle = |\phi\rangle, \quad |1\rangle = \tilde{H}|0\rangle, \quad |n+1\rangle = 2\tilde{H}|n\rangle - |n-1\rangle. \quad (46)$$

Each new vector requires only a sparse matrix–vector multiplication and a vector subtraction, making the method both efficient and numerically stable. In practice, the series is truncated at finite order to reach the desired accuracy and evaluated using the Clenshaw algorithm [75].

C.3 Numerical generation of the energy-resolved state

We first show how the Chebyshev method is used to numerically generate the energy-resolved state $|\psi_0\rangle$, defined by Eq. (2). In this problem, one applies the operator $\mathcal{F}(\hat{H}) = f(\hat{H} - E_f)$ to the BEC state $|\phi\rangle$ prior to transfer, where f is the filter function discussed in the main text. In this case, we use $|\psi_0\rangle = \mathcal{F}(\hat{H})|\phi\rangle = c_0|0\rangle + 2\sum_{n=1}^{\infty} c_n|n\rangle$, where the coefficients c_n are computed from Eq. (45). The integral defining c_n in Eq. (45) is conveniently evaluated by introducing the change of variable $\varepsilon = \cos\theta$. Using the identity $T_n(\varepsilon) = \cos(n \arccos \varepsilon)$, the coefficients can be written as the cosine transform

$$c_n = \frac{1}{\pi} \int_0^\pi \mathcal{F}(\cos\theta) \cos(n\theta) d\theta. \quad (47)$$

Numerically, the variable θ is sampled uniformly in the interval $(0, \pi)$ with N points, $\theta_k = (2k+1)\pi/(2N)$ ($0 \leq k \leq N-1$), and the integral is approximated by the discrete cosine transform

$$c_n \approx \frac{\Delta\theta}{\pi} \sum_{k=0}^{N-1} h_k \cos\left[n \frac{(2k+1)\pi}{2N}\right], \quad (48)$$

where $\Delta\theta = \pi/N$ and $h_k = \mathcal{F}(\cos\theta_k)$.

C.4 Numerical generation of the spectral function

The computation of the energy distribution $\mathcal{D}_{\text{BEC}} = F(E - E_f)A(E, \mathbf{k} = 0)$ appearing in Eq. (25) requires the numerical evaluation of the spectral function $A(E, \mathbf{k} = 0)$. This is performed using a Chebyshev expansion with $\mathcal{F}(\hat{H}) = \delta(E - \hat{H})$. To this end, we write:

$$A(E, \phi) \equiv \langle \phi | \delta(E - \hat{H}) | \phi \rangle = \langle \phi | \delta\left[\frac{E_{\max} - E_{\min}}{2}(\varepsilon - \tilde{H})\right] | \phi \rangle = \frac{2\tilde{A}(\varepsilon, \phi)}{E_{\max} - E_{\min}}, \quad (49)$$

where

$$\tilde{A}(\varepsilon, \phi) = \langle \phi | \delta(\varepsilon - \tilde{H}) | \phi \rangle \quad (50)$$

is the spectral function for the rescaled Hamiltonian, and we have introduced $|\phi\rangle = |\mathbf{k} = 0\rangle$. Using the Chebyshev expansion of the Dirac distribution [Eq. (44)], we obtain

$$\tilde{A}(\varepsilon, \phi) = c_0(\varepsilon) \langle \phi | 0 \rangle + 2 \sum_{n=1}^{\infty} c_n(\varepsilon) \langle \phi | n \rangle \quad \text{with} \quad c_n(\varepsilon) = \frac{T_n(\varepsilon)}{\pi\sqrt{1-\varepsilon^2}}. \quad (51)$$

To suppress Gibbs oscillations arising from truncation at finite order N , the coefficients are multiplied by Jackson weights. This procedure—equivalent to convolving the spectral function with an optimal smoothing kernel—is known as the Kernel Polynomial Method [74]. For the energy distributions shown in Fig. 5, we use $N = 10^4$, ensuring that the Jackson broadening remains well below the intrinsic width of the filtered spectral functions (below 1% for the narrowest spectral function of 4 Hz).

C.5 Time evolution

The initial state is propagated in time with step Δt according to $|\psi(t + \Delta t)\rangle = \exp(-i\hat{H}\Delta t)|\psi(t)\rangle$. Numerically, the evolution operator is applied efficiently using a Chebyshev expansion with $\mathcal{F}(\hat{H}) = \exp(-i\hat{H}\Delta t)$ [57]. To this end, the evolution operator is first rewritten as

$$\hat{U} = \exp(-iE_{\text{mid}}\Delta t) \exp(-i\tilde{H}\Delta\tilde{t}) = \exp(-iE_{\text{mid}}\Delta t) \tilde{U}, \quad (52)$$

where $\Delta\tilde{t} = (E_{\max} - E_{\min})\Delta t/2$. The first factor in Eq. (52) is a global phase, which leads to an irrelevant energy shift and has no impact on the dynamics. The second factor, denoted \tilde{U} , can be expanded as

$$\tilde{U} = \int_{-1}^1 \delta(\varepsilon - \tilde{H}) \exp(-i\varepsilon\Delta\tilde{t}) d\varepsilon = c_0(\Delta\tilde{t})T_0(\tilde{H}) + 2 \sum_{n=1}^{\infty} c_n(\Delta\tilde{t})T_n(\tilde{H}), \quad (53)$$

where Eq. (44) has been used in the second equality. The coefficients $c_n(\Delta\tilde{t})$ are given in closed form as

$$c_n(\Delta\tilde{t}) = \int_{-1}^1 \frac{\exp(-i\varepsilon\Delta\tilde{t})}{\pi\sqrt{1-\varepsilon^2}} T_n(\varepsilon) d\varepsilon = (-i)^n J_n(\Delta\tilde{t}), \quad (54)$$

where J_n denotes the Bessel function of the first kind of order n . Applying the evolution operator thus amounts to computing

$$|\psi(t + \Delta t)\rangle = \exp(-iE_{\text{mid}}\Delta t) \left[c_0(\Delta\tilde{t}) |0\rangle + 2 \sum_{n=1}^{\infty} c_n(\Delta\tilde{t}) |n\rangle \right], \quad (55)$$

where the vectors $|n\rangle = T_n(\tilde{H}) |\psi(t)\rangle$ are generated recursively using Eq. (46). Owing to the rapid decay of the Bessel functions with n , the series can be safely truncated without additional regularization.

Acknowledgments

The authors thank V. Denechaud, B. Lecoutre, A. Signoles for early work and D. Clément, D. Delande and M. Filoche for fruitful discussions.

Funding

This work benefited financial support from the project Localization of Waves of the Simons Foundation (Grant No. 601939), the French National Research Agency under Grant No. ANR-24-CE30-6695 (FUSIoN), Grant No. ANR-25-CPJ1-0059-01 (CPJ LUMIS), Grant No. ANR-22-CMAS-0001(QuanTEdu-France) and Region Île-de-France in the framework of DIM QuanTiP.

Author contributions

J.-P. B., S. B. and N. C. conducted the numerical simulations and developed the theoretical predictions. K. X., H.-M. Q., X. Y., M. N. and Y. G. carried out the experiments. All authors contributed to data analysis, project development, and the writing of the paper.

Data availability

All numerical data presented in this work are available under reasonable request.

References

- [1] P. A. Lee and T. V. Ramakrishnan. Disordered electronic systems. *Reviews of Modern Physics*, 57(2):287–337, 1985.
- [2] A. Lagendijk, B. van Tiggelen, and D. S. Wiersma. Fifty years of anderson localization. *Physics Today*, 62(8):24–29, 2009.
- [3] A. Aspect and M. Inguscio. Anderson localization of ultracold atoms. *Physics Today*, 62(8):30, 2009.
- [4] P. W. Anderson. Absence of diffusion in certain random lattices. *Physical Review*, 109(5):1492–1505, 1958.
- [5] E. Abrahams, P. W. Anderson, D. C. Licciardello, and T. V. Ramakrishnan. Scaling theory of localization: Absence of quantum diffusion in two dimensions. *Physical Review Letters*, 42(10):673–676, 1979.
- [6] E. Abrahams. *50 years of Anderson Localization*. World Scientific, 2010.
- [7] D. Clément, A. F Varòn, J. A Retter, L. Sanchez-Palencia, A. Aspect, and P. Bouyer. Experimental study of the transport of coherent interacting matter-waves in a 1D random potential induced by laser speckle. *New Journal of Physics*, 8(8):165, 2006.
- [8] L. Sanchez-Palencia and M. Lewenstein. Disordered quantum gases under control. *Nature Physics*, 6(2):87–95, 2010.
- [9] C. A. Müller and D. Delande. Disorder and interference: localization phenomena. In *Ultracold Gases and Quantum Information: Lecture Notes of the Les Houches Summer School in Singapore: Volume 91, July 2009*. Oxford University Press, 05 2011.

- [10] B. Shapiro. Cold atoms in the presence of disorder. *Journal of Physics A: Mathematical and Theoretical*, 45(14):143001, 2012.
- [11] N. Cherroret, T. Scoquart, and D. Delande. Coherent multiple scattering of out-of-equilibrium interacting bose gases. *Annals of Physics*, 435:168543, 2021. Special Issue on Localisation 2020.
- [12] L. Sanchez-Palencia, D. Clément, P. Lugan, P. Bouyer, G. V. Shlyapnikov, and A. Aspect. Anderson localization of expanding Bose-Einstein condensates in random potentials. *Physical Review Letters*, 98:210401, May 2007.
- [13] S. E. Skipetrov, A. Minguzzi, B. A. van Tiggelen, and B. Shapiro. Anderson localization of a Bose-Einstein condensate in a 3d random potential. *Physical Review Letters*, 100(16):165301, 2008.
- [14] P. Lugan, A. Aspect, L. Sanchez-Palencia, D. Delande, B. Grémaud, C. A. Müller, and C. Miniatura. One-dimensional anderson localization in certain correlated random potentials. *Phys. Rev. A*, 80:023605, Aug 2009.
- [15] M. Filoche and S. Mayboroda. Universal mechanism for Anderson and weak localization. *Proceedings of the National Academy of Sciences of the United States of America*, 109(37):14761–14766, 2012.
- [16] M. Piraud, L. Pezzé, and L. Sanchez-Palencia. Matter wave transport and anderson localization in anisotropic three-dimensional disorder. *Europhysics Letters*, 99(5):50003, sep 2012.
- [17] T. Karpiuk, N. Cherroret, K. L. Lee, B. Grémaud, C. A. Müller, and C. Miniatura. Coherent forward scattering peak induced by Anderson localization. *Physical Review Letters*, 109:190601, Nov 2012.
- [18] T. Plisson, T. Bourdel, and C. A. Müller. Momentum isotropisation in random potentials. *The European Physical Journal Special Topics*, 217(1):79–84, 2013.
- [19] M. Piraud, L. Sanchez-Palencia, and B. van Tiggelen. Anderson localization of matter waves in three-dimensional anisotropic disordered potentials. *Physical Review A*, 90(6):063639, 2014.
- [20] D. Delande and G. Orso. Mobility edge for cold atoms in laser speckle potentials. *Physical Review Letters*, 113(6):060601, 2014.
- [21] E. Fratini and S. Pilati. Anderson localization of matter waves in quantum-chaos theory. *Physical Review A*, 91(6):061601, 2015.
- [22] C. A. Müller, D. Delande, and B. Shapiro. Critical dynamics at the Anderson localization mobility edge. *Physical Review A*, 94(3):033615, 2016.
- [23] M. Pasek, G. Orso, and D. Delande. Anderson localization of ultracold atoms: Where is the mobility edge? *Physical Review Letters*, 118(17):170403, 2017.
- [24] G. Lemarié. Glassy properties of anderson localization: Pinning, avalanches, and chaos. *Phys. Rev. Lett.*, 122:030401, Jan 2019.
- [25] M. Filoche, P. Pelletier, D. Delande, and S. Mayboroda. Anderson mobility edge as a percolation transition. *Physical Review B*, 109(22):L220202, 2024.
- [26] M. Vrech, J. Major, D. Delande, M. Filoche, and N. Cherroret. From percolation transition to anderson localization in one-dimensional speckle potentials. *New Journal of Physics*, 28(2):024508, 2026.
- [27] J. Billy, V. Josse, Z. Zuo, A. Bernard, B. Hambrecht, P. Lugan, D. Clément, L. Sanchez-Palencia, P. Bouyer, and A. Aspect. Direct observation of anderson localization of matter waves in a controlled disorder. *Nature*, 453(7197):891–894, 2008.
- [28] G. Roati, C. D’Errico, L. Fallani, M. Fattori, C. Fort, M. Zaccanti, G. Modugno, M. Modugno, and M. Inguscio. Anderson localization of a non-interacting Bose-Einstein condensate. *Nature*, 453:895–898, 2008.

- [29] D. H. White, T. A. Haase, D. J. Brown, M. D. Hoogerland, M. S. Najafabadi, J. L. Helm, C. Gies, D. Schumayer, and D. A. W. Hutchinson. Observation of two-dimensional anderson localisation of ultracold atoms. *Nature Communications*, 11:4942, 2020.
- [30] S. S. Kondov, W. R. McGehee, J. J. Zirbel, and B. DeMarco. Three-dimensional anderson localization of ultracold matter. *Science*, 334(6052):66–68, 2011.
- [31] F. Jendrzejewski, A. Bernard, K. Müller, P. Cheinet, V. Josse, M. Piraud, L. Pezzé, L. Sanchez-Palencia, A. Aspect, and P. Bouyer. Three-dimensional localization of ultracold atoms in an optical disordered potential. *Nature Physics*, 8(5):398–403, 2012.
- [32] G. Semeghini, M. Landini, P. Castilho, S. Roy, G. Spagnolli, A. Trenkwalder, M. Fattori, M. Inguscio, and G. Modugno. Measurement of the mobility edge for 3d Anderson localization. *Nature Physics*, 11(7):554–559, 2015.
- [33] S. Barbosa, M. Kiefer-Emmanouilidis, F. Lang, J. Koch, and A. Widera. Characterizing localization effects in an ultracold disordered fermi gas by diffusion analysis. *Physical Review Research*, 6(3):033039, 2024.
- [34] F. L. Moore, J. C. Robinson, C. F. Bharucha, B. Sundaram, and M. G. Raizen. Atom optics realization of the quantum δ -kicked rotor. *Physical Review Letters*, 75(25):4598–4601, 1995.
- [35] J. Chabé, G. Lemarié, B. Grémaud, D. Delande, P. Szriftgiser, and J. C. Garreau. Experimental observation of the anderson metal-insulator transition with atomic matter waves. *Physical Review Letters*, 101(25):255702, 2008.
- [36] C. Hainaut, I. Manai, R. Chicireanu, J.-F. Clément, S. Zemmouri, J.-C. Garreau, P. Szriftgiser, G. Lemarié, N. Cherroret, and D. Delande. Return to the origin as a probe of atomic phase coherence. *Physical Review Letters*, 118(18):184101, 2017.
- [37] C. Hainaut, I. Manai, J.-F. Clément, J.-C. Garreau, P. Szriftgiser, G. Lemarié, N. Cherroret, D. Delande, and R. Chicireanu. Controlling symmetry and localization with an artificial gauge field in a disordered quantum system. *Nature Communications*, 9(1):1382, 2018.
- [38] F. Arrouas, J. Hébraud, N. Ombredane, E. Flament, D. Ronco, N. Dupont, G. Lemarié, B. Georgeot, C. Miniatura, J. Billy, B. Peaudecerf, and D. Guéry-Odelin. Probing non-ergodicity and symmetry via coherent forward scattering in a shaken rotor. *arXiv:2503.01777*, 2025.
- [39] F. Madani, M. Denis, P. Szriftgiser, J.-C. Garreau, A. Raçon, and R. Chicireanu. Observation of quantum criticality of a four-dimensional phase transition. *Nature Communications*, 16(1), 2025.
- [40] X. Yu, K. Xie, H.-M. Quach, Y. Guo, N. Myneni, S. Barré, J.-P. Banon, A. Aspect, N. Cherroret, and V. Josse. Direct observation of the three-dimensional anderson transition with ultracold atoms in a disordered potential. *arXiv:2602.07654*, 2026.
- [41] V. V. Volchkov, M. Pasek, V. Denechaud, M. Mukhtar, A. Aspect, D. Delande, and V. Josse. Measurement of spectral functions of ultracold atoms in disordered potentials. *Physical Review Letters*, 120(6):060404, 2018.
- [42] B. Lecoutre, Y. Guo, X. Yu, M. Niranjana, M. Mukhtar, V. V. Volchkov, A. Aspect, and V. Josse. Bichromatic state-dependent disordered potential for anderson localization of ultracold atoms. *The European Physical Journal D*, 76(11), November 2022.
- [43] D. Vollhardt and P. Wölfle. Anderson localization in $d \lesssim 2$ dimensions: A self-consistent diagrammatic theory. *Physical Review Letters*, 45:842–846, Sep 1980.
- [44] D. Vollhardt and P. Wölfle. Diagrammatic, self-consistent treatment of the anderson localization problem in $d \leq 2$ dimensions. *Physical Review B*, 22:4666–4679, Nov 1980.
- [45] P. Wölfle and D. Vollhardt. Self-consistent theory of anderson localization: General formalism and applications. *International Journal of Modern Physics B*, 24(12n13):1526–1554, May 2010.

- [46] N. Cherroret. A self-consistent theory of localization in nonlinear random media. *Journal of Physics: Condensed Matter*, 29(2):024002, 2016.
- [47] E. Akkermans and G. Montambaux. *Mesoscopic Physics of Electrons and Photons*. Cambridge University Press, 2007.
- [48] O. I. Lobkis and R. L. Weaver. Self-consistent transport dynamics for localized waves. *Physical Review E*, 71(1):011112, 2005.
- [49] N. Cherroret. Localization phenomena in quantum disordered systems: from electrons to cold atoms, 2025. Lecture notes, Sorbonne Université / ENS Paris (HAL: hal-05429222v1).
- [50] R. C. Kuhn, O. Sigwarth, C. Miniatura, D. Delande, and C. A. Müller. Coherent matter wave transport in speckle potentials. *New Journal of Physics*, 9(6):161, 2007.
- [51] J. Richard, L.-K. Lim, V. Denechaud, V. V. Volchkov, B. Lecoutre, M. Mukhtar, F. Jendrzejewski, A. Aspect, A. Signoles, L. Sanchez-Palencia, et al. Elastic scattering time of matter waves in disordered potentials. *Physical Review Letters*, 122(10):100403, 2019.
- [52] B. Shapiro. Self-consistent calculation of the frequency-dependent conductivity near the anderson transition. *Physical Review B*, 25(6):4266–4269, 1982.
- [53] T. Ohtsuki and T. Kawarabayashi. Anomalous diffusion at the anderson transitions. *Journal of the Physical Society of Japan*, 66(2):314–317, 1997.
- [54] S. Ghosh, N. Cherroret, B. Grémaud, C. Miniatura, and D. Delande. Coherent forward scattering in two-dimensional disordered systems. *Physical Review A*, 90(6):063602, 2014.
- [55] S. Ghosh, D. Delande, C. Miniatura, and N. Cherroret. Coherent backscattering reveals the anderson transition. *Physical Review Letters*, 115(20):200602, 2015.
- [56] S. Ghosh, C. Miniatura, N. Cherroret, and D. Delande. Coherent forward scattering as a signature of Anderson metal-insulator transitions. *Physical Review A*, 95(4):041602, 2017.
- [57] H. Fehske, J. Schleede, G. Schubert, G. Wellein, V. S. Filinov, and A. R. Bishop. Numerical approaches to time evolution of complex quantum systems. *Physics Letters A*, 373(25):2182–2188, 2009.
- [58] S. Roche and D. Mayou. Conductivity of quasiperiodic systems: A numerical study. *Physical Review Letters*, 79(13):2518–2521, 1997.
- [59] G. Lemarié, J. Chabé, P. Szriftgiser, J. C. Garreau, B. Grémaud, and D. Delande. Observation of the anderson metal-insulator transition with atomic matter waves: Theory and experiment. *Physical Review A*, 80(4):043626, 2009.
- [60] P. Akridas-Morel, N. Cherroret, and D. Delande. Multifractality of the kicked rotor at the critical point of the anderson transition. *Physical Review A*, 100(4):043612, 2019.
- [61] V. I. Korepanov and D. M. Sedlovets. An asymmetric fitting function for condensed-phase raman spectroscopy. *Analyst*, 143(11):2674–2679, 2018.
- [62] C. A. Müller and B. Shapiro. Comment on “three-dimensional anderson localization in variable scale disorder”. *Physical Review Letters*, 113(9):099601, 2014.
- [63] N. Cherroret, B. Vermersch, J.-C. Garreau, and D. Delande. How nonlinear interactions challenge the three-dimensional Anderson transition. *Physical Review Letters*, 112(17):170603, 2014.
- [64] A. D. Mirlin. Statistics of energy levels and eigenfunctions in disordered systems. *Physics Reports*, 326(5):259–382, 2000.
- [65] A. D. Mirlin and F. Evers. Multifractality and critical fluctuations at the anderson transition. *Physical Review B*, 62(12):7920–7933, 2000.

- [66] L. Pezzé, M. Robert-de Saint-Vincent, T. Bourdel, J.-P. Brantut, B. Allard, T. Plisson, A. Aspect, P. Bouyer, and L. Sanchez-Palencia. Regimes of classical transport of cold gases in a two-dimensional anisotropic disorder. *New Journal of Physics*, 13(9):095015, sep 2011.
- [67] F. Jendrzejewski, K. Müller, J. Richard, A. Date, T. Plisson, P. Bouyer, A. Aspect, and V. Josse. Coherent backscattering of ultracold atoms. *Physical Review Letters*, 109(19):195302, 2012.
- [68] E. Arabahmadi, D. Schumayer, B. Grémaud, C. Miniatura, and D. A. W. Hutchinson. Momentum-space signatures of the anderson transition in a symplectic, two-dimensional, disordered ultracold gas. *Phys. Rev. Res.*, 6:L012021, Jan 2024.
- [69] J. Biddle and S. Das Sarma. Predicted mobility edges in one-dimensional incommensurate optical lattices: An exactly solvable model of Anderson localization. *Physical Review Letters*, 104(7):070601, 2010.
- [70] H. P. Lüschen, S. Scherg, T. Kohlert, M. Schreiber, P. Bordia, X. Li, S. Das Sarma, and I. Bloch. Single-particle mobility edge in a one-dimensional quasiperiodic optical lattice. *Physical Review Letters*, 120(16):160404, 2018.
- [71] F. A. An, K. Padavić, E. J. Meier, S. Hegde, S. Ganeshan, J. H. Pixley, S. Vishveshwara, and B. Gadway. Interactions and mobility edges: Observing the generalized Aubry-André model. *Phys. Rev. Lett.*, 126:040603, Jan 2021.
- [72] Y. Wang, J.-H. Zhang, Y. Li, J. Wu, W. Liu, F. Mei, Y. Hu, L. Xiao, J. Ma, C. Chin, and S. Jia. Observation of interaction-induced mobility edge in an atomic Aubry-André wire. *Physical Review Letters*, 129(10):103401, 2022.
- [73] J. W. Goodman. *Speckle Phenomena in Optics: Theory and Applications*. Roberts and Company Publishers, 2007.
- [74] A. Weiße, G. Wellein, A. Alvermann, and H. Fehske. The kernel polynomial method. *Reviews of Modern Physics*, 78(1):275–306, 2006.
- [75] C. W. Clenshaw. A note on the summation of Chebyshev series. *Mathematics of Computation*, 9(51):118–120, 1955.